energies

MDPI

Article

Energy Management for PV Powered Hybrid Storage System in Electric Vehicles Using Artificial Neural Network and Aquila Optimizer Algorithm

Namala Narasimhulu [1], R. S. R. Krishnam Naidu [2], Przemysław Falkowski-Gilski [3,*], Parameshachari Bidare Divakarachari [4,*] and Upendra Roy [5]

[1] Department of Electrical and Electronics Engineering, Srinivasa Ramanujan Institute of Technology (Autonomous), Ananthapuramu 515701, Andhra Pradesh, India
[2] Department of Electrical and Electronics Engineering, N S Raju Institute of Technology, Sontyam, Visakhapatnam 531173, Andhra Pradesh, India
[3] Faculty of Electronics, Telecommunications and Informatics, Gdansk University of Technology, Narutowicza 11/12, 80-233 Gdansk, Poland
[4] Department of Electronics and Communication Engineering, Nitte Meenakshi Institute of Technology, Bangalore 560064, Karnataka, India
[5] Department of Electrical and Electronics Engineering, Channabasaveshwara Institute of Technology, Tumkur 572216, Karnataka, India
* Correspondence: przemyslaw.falkowski@eti.pg.edu.pl (P.F.-G.); paramesh@nmit.ac.in (P.B.D.)

Abstract: In an electric vehicle (EV), using more than one energy source often provides a safe ride without concerns about range. EVs are powered by photovoltaic (PV), battery, and ultracapacitor (UC) systems. The overall results of this arrangement are an increase in travel distance; a reduction in battery size; improved reaction, especially under overload; and an extension of battery life. Improved results allow the energy to be used efficiently, provide a comfortable ride, and require fewer energy sources. In this research, energy management between the PV system and the hybrid energy storage system (HESS), including the battery, and UC are discussed. The energy management control algorithms called Artificial Neural Network (ANN) and Aquila Optimizer Algorithm (AOA) are proposed. The proposed combined ANN–AOA approach takes full advantage of UC while limiting the battery discharge current, since it also mitigates high-speed dynamic battery charging and discharging currents. The responses' behaviors are depicted and viewed in the MATLAB simulation environment to represent load variations and various road conditions. We also discuss the management among the PV system, battery, and UC to achieve the higher speed of 91 km/h when compared with existing Modified Harmony Search (MHS) and Genetic Algorithm-based Proportional Integral Derivative (GA-PID). The outcomes of this study could aid researchers and professionals from the automotive industry as well as various third parties involved in designing, maintaining, and evaluating a variety of energy sources and storage systems, especially renewable ones.

Keywords: Artificial Neural Network; Aquila Optimizer Algorithm; battery; hybrid energy storage system; photo-voltaic system; ultracapacitor

check for updates

Citation: Narasimhulu, N.; Krishnam Naidu, R.S.R.; Falkowski-Gilski, P.; Divakarachari, P.B.; Roy, U. Energy Management for PV Powered Hybrid Storage System in Electric Vehicles Using Artificial Neural Network and Aquila Optimizer Algorithm. *Energies* **2022**, *15*, 8540. https://doi.org/10.3390/en15228540

Academic Editor: GM Shafiullah

Received: 4 October 2022
Accepted: 10 November 2022
Published: 15 November 2022

Publisher's Note: MDPI stays neutral with regard to jurisdictional claims in published maps and institutional affiliations.

1. Introduction

Due to technological innovations in storage, adjustable speed drives, etc., the appeal of electric vehicles (EVs) has increased recently [1,2]. The EV has fewer components than traditional fossil fuel-powered automobiles. It has many benefits, such as being extremely durable, quiet, and environmentally beneficial, among others [3]. In order to provide a consistent supply of electricity for a longer distance, more than one electrical energy source is recommended in EVs. In numerous nations, commercial solar-powered electric vehicles have been introduced for public usage [4]. They utilize the battery as a storage device to power an electric vehicle equipped with solar panels. While using multiple energy sources,

a power electronic conversion is crucial in integrating the sources and supplying the EV with power in accordance with its needs [5,6]. This pattern is also indicated by recently proposed promotional initiatives from host agencies. Such a system is presented in [7], which uses a battery, an ultracapacitor (UC), and an engine turbine as its energy sources. Although, there are no emissions, the effectiveness is constrained for sophisticated power electronic systems. In [8], an all-electric vehicle energy infrastructure is described that utilizes UC as its sole and special energy source.

Overall, UC offers excellent characteristics throughout a range of temperatures [9], excellent specific energy, relatively low impedance, quick charging using high current, and ideal characteristics. Furthermore, it may discharge deeply and has a lengthy life span. However, the issue is that it has a low energy density, which limits its travel distance [10,11]. Experts are working to increase the ultracapacitor's power density so that it may function like a battery. However, combining the battery with a supercapacitor in a vehicle, in which each component executes its respective task based on its unique features, is a more realistic solution [12,13].

In [14], the authors describe centralized converters for integrating the input sources, whereas in [15], there is no feasible way to use the bi-directional power flow to recover energy from regenerative braking. Electricity from the input data is consistently implemented to the loads using an appropriate switching mechanism by the input sources [16]. Because the input resources are placed in a feedforward pattern, some transistors do, nevertheless, face higher voltage strains. In [17], the load can receive the power from the inputs, whether concurrently or sequentially. According to the given structure [18], recharging the input source 1 from the source 2 is not allowed. Therefore, the converter must have a variety of operational characteristics in buck or boost, based on the type of implementations, output and input, etc. [19,20]. In order to overcome those problems, a novel method called Artificial Neural Network and Aquila Optimizer Algorithm (ANN–AOA) is proposed in this paper. The major contribution of this research is as follows:

- The distribution of energy among the PV system, batteries, and UCs is suggested using an energy management strategy (EMS).
- A hybrid energy storage system (HESS) architecture that stores PV energy utilizing batteries and UCs is proposed.
- The ANN–AOA technique of managing the DC bus voltage and the buck-boost converter current is presented. The DC bus voltage can be stabilized by offering a control technique.
- An evaluation of the various topologies utilized to interface the load with the batteries and UCs is discussed. Various models are used to describe this analysis, which details the benefits and drawbacks of every structure.

The paper is organized as follows: Section 1 provides an introduction to the discussed topic. Section 2 presents a review of related works. Section 3 refers to modeling of available resources in an energy system. Section 4 describes the proposed method. Section 5 defines the AOA method. Section 6 presents the results along with discussions on obtained outcomes. Section 7 concludes this paper.

2. Literature Review

For better solar vehicle traction system performance, Cabranea et al. [21] showed the modelling and simulation experiments of a battery–super-capacitor HESS. In this research, the combination of SCs and batteries ensured the power control of the electric traction network of the PV car to reduce the impact of peak current requirements on the battery driving conditions. The experiment findings showed that the SC's incorporation into the PV car's energy storage system was successful in reducing battery stressors and removing peak current flow in the rechargeable battery. This tended to result in an extended battery life, even though certain voltage and current sensing losses occurred as a result of the designed sensors' limited capabilities in the processor.

With a PV-powered EV outfitted with a battery and SC, Savrun and Atay [22] presented a multiport bi-directional DC/DC converter. The suggested topology was capable of bi-directional power flow and offered continuous power to the EV motor while recovering braking energy. The system incorporated H-bridge converters and quasi-Z-sources with an existing switch. The recommended design, unfortunately, only offered restricted voltage gain into the HFTs' turns proportion and necessitated more circuits in order to add more connections.

Depending on heuristic techniques, Guentri et al. [23] showed how to manage and control the energy of a solar panel using hybrid battery–SC energy storage. The purpose of this study was to modify the HES's voltage regulation architecture to accommodate these strong control principles. The performance metrics and reliability of these approaches were also evaluated. Under varying solar irradiation and load circumstances, the effectiveness and stability of these devices and the battery management technique to synchronize between the batteries and SC were indeed evaluated, and numerous simulated scenarios were provided. Peak overshoot and settling time were significantly reduced by the GA optimization technique, resulting in enhanced efficiency. With the GA-based proportional integral derivative (PID) controller design, the machine became problematic only after the threshold of 67%.

A novel multiport DC/DC converter was presented by Sumner et al. [24] for improving the development and performance of battery–SC HESS. The essential concept of the control method for HESS is that the battery provides the low-frequency power/high energy component, while the SC serves the high frequency/high amplitude elements of the load power, which are typically approximated by a load voltage regulator. The inductors' current fluctuations were further decreased by suggesting the adoption of a phase-shifted carrier modulation approach, allowing for an additional decrease in inductor capacity. However, the SC's permitted voltage range was constrained by the higher transistor count and the fact that voltage boosting was permitted at the source side.

The implementation and quality assessment of an integrated battery and UC energy storage for EV was conducted by Kachhwaha et al. [25]. According to the analytical model, the benefit of this configuration is that it effectively controls the DC link voltage of an electric vehicle with a hybrid power source while placing the battery under the least amount of load stress possible, extending the battery lifetime. By putting less strain on the battery, the suggested HESS active power system provided effective and better control during the EV's driving operation. Due to the ultracapacitor's performance being significantly decreased, namely, beneath the level of state of charge (SOC), its value was approx. equal to 50%. The SOC guidelines for batteries have been modified in accordance with industry and user needs.

An effective short-term energy management plan for a micro grid with EV and renewable electricity production was established by Al-Dhaifallah et al. [26]. Three different charging methods, including unsupervised, supervised, and smart charging techniques, were taken into consideration in order to evaluate the behavior of EVs. In micro grid modeling power systems, constraints resulting from estimates in PHEVs, loads, pricing, and energy resource power density are often taken into account. A modified harmony search (MHS) method was applied to cope with the optimization planning of micro grids while taking uncertainty into consideration. Even though the MG's Day-ahead planning was a crucial issue, it requires serious consideration.

Katuri and Gorantla [27] showed how to apply a math function-based (MFB) controller with PI and PID to an EV driven by solar energy using ultracapacitors. By designing a novel control system that included two distinct processors, the EV issue was overcome in this application. A new control, known as an MFB controller, was developed using four distinct mathematical operations, depending on the coding, and using a speed value as a baseline. The MFB was also combined with a conventional controller to create a hybrid controller (HC), which switched the energy sources to complement the velocity of the motor. The charging rate and discharge rate were managed based on the solar energy's accessibility. These did not deliver effective outcomes such as those of IC engine automobiles and were not straightforward.

In order to integrate renewable resources, Suresh et al. [28] used a modular multi-input bi-directional DC/DC buck-boost converter. The suggested four-port converter was implemented with a lower component count and a more straightforward control scheme, which increased the converter's dependability and efficiency. Additionally, this converter featured bi-directional power flow capability, which qualified it for use in an electric brake to charge the battery. Power converters with buck-boost capabilities are used in all EV power trains to handle the bi-directional power flow between the vehicle drive and the energy supplies, even though the DC bus power cannot be adjusted for EV applications of this converter.

3. Modelling of Resources

An intelligent energy system is typically composed of the three subsystems of production, storage, and load. Depending on specific factors, such as the availability of renewable resources, the services to be delivered, and the energy consumption profile, these components may vary significantly. These are primarily the crucial variables that have an important bearing on the design and optimization of the entire system. The combination of various power sources and the use of high-quality parts also significantly affects the system's effectiveness and lifespan and can lower the cost of electricity for customers in remote places.

3.1. Modelling the PV

Solar cells have a P–N junction, which aids in the conversion of solar energy into DC electricity. The PV model's equivalent circuit can be classified into two types: single diode and double diode. For design and simulation investigations, the single diode model is preferred. PV power is also primarily determined by high temperatures, production factors, and geographic regions. The voltage and capacity of a PV system is defined by interconnecting the PV panels in parallel or series [29]. In order to increase the maximum power point (MPP), the maximum power point tracking (MPPT) technique is used in the solar panel [30]. The PV cell's V-I characteristics are shown in Figure 1.

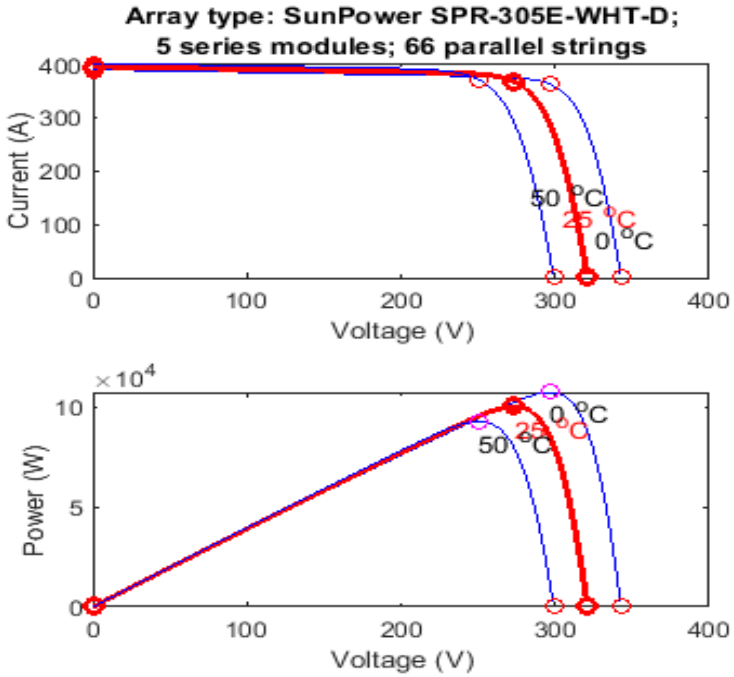

Figure 1. V-I characteristics of a PV cell.

Equation (1) depends on the I_M and V_M, which denote the maximum current and maximum voltage, respectively:

$$P_{MPPT}(t) = I_{MPPT}(t) \times V_{MPPT}(t) \quad (1)$$

The current and voltage of MPPT are given in Equations (2) and (3), respectively:

$$I_{MPPT}(t) = I_{SC}\left\{1 - C_1\left[exp\left(\frac{V_M}{C_2 \times V_{OC}}\right)\right]\right\} + \Delta I(t) \quad (2)$$

$$V_{MPPT}(t) = V_M + \mu V_{OC} \cdot \Delta T(t) \quad (3)$$

where V_{OC} and I_{SC} are stated as open circuit voltage and short circuit current, respectively; capacitances are represented as C_1 and C_2; the voltage at maximum level is designated as V_M; and where C_1, C_2, $\Delta I(t)$ and $\Delta T(t)$ of (2) and (3) are defined in (4)–(7), correspondingly [31].

$$C_1 = \left(1 - \frac{I_M}{I_{SC}}\right) \times exp\left(-\frac{V_M}{C_2 \times V_{OC}}\right) \quad (4)$$

$$C_2 = \left(\frac{V_M}{V_{OC}} - 1\right) \times \left[ln\left(1 - \frac{I_M}{I_{SC}}\right)\right]^{-1} \quad (5)$$

$$\Delta I(t) = I_{SC}\left(\frac{GT(t)}{G_{ref}} - 1\right) + \alpha_{1,sc} \times \Delta T(t) \quad (6)$$

$$\Delta T(t) = T_c(t) - T_{c,ref} \quad (7)$$

3.2. Modelling the Battery

The modelling of the battery [32] is shown in Figure 2.

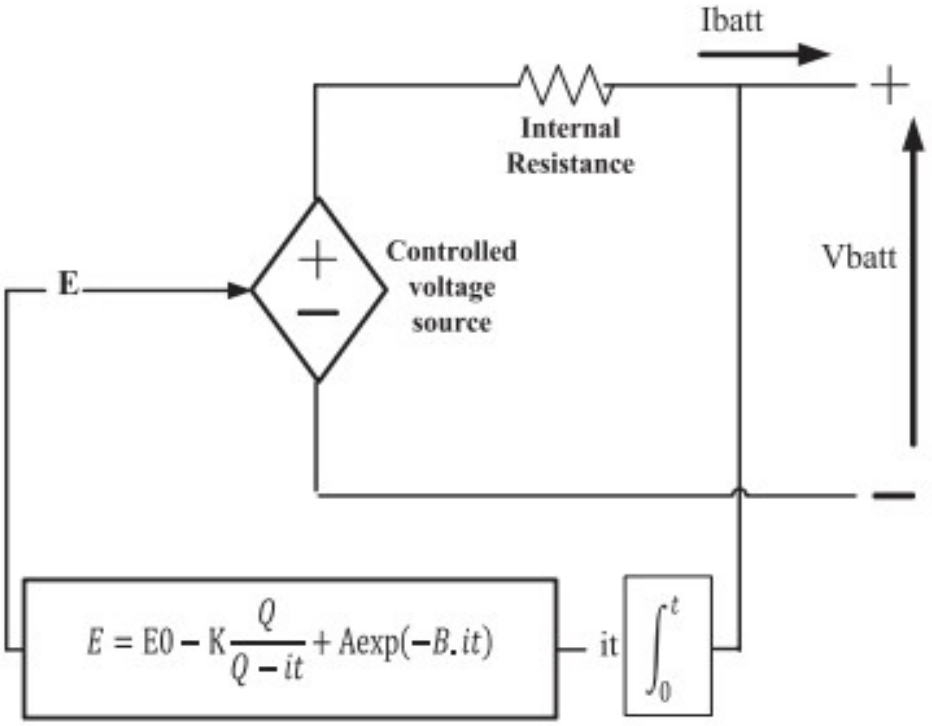

Figure 2. Model of the battery.

The battery voltage V_{bat} is given in Equation (8):

$$V_{bat} = E - R_{bat} * I_{bat} \quad (8)$$

The controlled voltage source is given in Equation (9):

$$E = E_0 - K\frac{Q}{(Q_D - \int idt)} + A.exp\,(-B\int idt) \quad (9)$$

where E represents the no load voltage (V), E_0 signifies the battery constant voltage (V), Q characterizes the battery capacity (Ah), A designates the exponential zone amplitude (V), K represents the polarization voltage (V), and B represents the exponential zone time constant inverse $(Ah)^{-1}$ [33].

3.3. Model the Ultracapacitor

The UC is referred to as one of the newest inventions for storing energy, particularly for fixed structures, as shown in Figure 3.

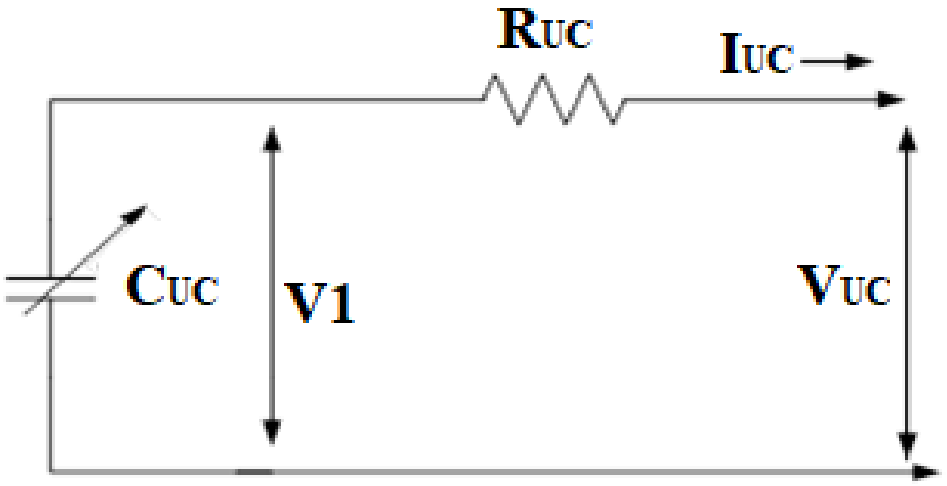

Figure 3. Model of an ultracapacitor.

The design comprises a capacitance C_{UC} in series through a corresponding series resistance R_{UC}. UC voltage V_{UC} is specified as the role of SC current I_{UC} defined by Equation (10):

$$V_{UC} = V_1 - R_{UC} \times I_{UC} = \frac{Q_{UC}}{C_{UC}} - R_{UC} \times I_{UC} \quad (10)$$

where Q_{UC} is specified as the amount of electricity kept in a cell. The power of UC is given in Equation (11):

$$P_{UC} = \frac{Q_{UC}}{C_{UC}} \times I_{UC} - R_{UC} \times I_{UC} \quad (11)$$

The capacity of UC and its resistance load are well-defined, correspondingly, by Equations (12) and (13):

$$C_{UC} = C_{elem}\frac{N_P}{N_S} \quad (12)$$

$$R_{UC} = R_{elem}\frac{N_s}{N_P} \quad (13)$$

The current and voltage of the load are assumed as the utility of the component voltage and the component current, respectively, and are expressed in Equations (14) and (15):

$$V_{UC} = N_s \cdot V_{elem} \quad (14)$$

$$I_{UC} = N_P \cdot I_{elem} \quad (15)$$

3.4. Modelling the PMSM

The modelling of a permanent magnet synchronous motor (PMSM) is based on the hypotheses that the stator resistances and the self-inductances of all windings are equal [34]. The stator phase voltage equation of a PMSM motor is similar to the armature equation of DC machines, which can be represented in a matrix form in Equation (16):

$$\begin{bmatrix} V_a \\ V_b \\ V_c \end{bmatrix} = R \begin{bmatrix} 1 & 0 & 0 \\ 0 & 1 & 0 \\ 0 & 0 & 1 \end{bmatrix} \begin{bmatrix} i_a \\ i_b \\ i_c \end{bmatrix} + \begin{bmatrix} L-M & 0 & 0 \\ 0 & L-M & 0 \\ 0 & 0 & L-M \end{bmatrix} \frac{d}{dt} \begin{bmatrix} i_a \\ i_b \\ i_c \end{bmatrix} + \begin{bmatrix} E_a \\ E_b \\ E_c \end{bmatrix} \quad (16)$$

where V_a, V_b and V_c represent the stator phase voltages, E_a, E_b and E_c are the trapezoidal back emf, i_a, i_b and i_c are the motor input currents, and R_a, R_b and R_c represent the terminal resistances. The L and M represent the self and mutual inductances, respectively. The electromagnetic torque of PMSM motor can be estimated by Equation (17):

$$T_e = \frac{P}{w_m} \quad (17)$$

where $P = E_a i_a + E_b i_b + E_c i_c$.

The electromagnetic torque of the PMSM motor in the synchronously rotating frames can be estimated as in (3).

$$T_e = \frac{3}{2}\frac{p_n}{2}[(\frac{dL_d}{d\theta_e} i_{sd} + \frac{d\varphi_{rd}}{d\theta_e} - \varphi_{sq}) i_{sd} + (\frac{dL_q}{d\theta_e} i_{sq} + \frac{d\varphi_{rq}}{d\theta_e} - \varphi_{sd}) i_{sq}] \quad (18)$$

where $\varphi_{sq} = L_q i_{sq} + \varphi_{rq}$ and $\varphi_{sd} = L_d i_{sd} + \varphi_{rd}$, in which p_n is the number of poles; i_{sd}, i_{sq}, L_d and L_q represent the d and q axes currents and inductances, respectively; θ_r represents the rotor angle; and φ_{rd}, φ_{rq}, φ_{sd} and φ_{sq} are the rotor and stator flux linkages in d and q axes, respectively. This electromagnetic torque equation can be simplified by converting it into a stationary $\alpha\beta$ frame, which is expressed as Equation (19):

$$T_e = \frac{3}{2}\frac{p_n}{2}[\frac{d\varphi_{r\alpha}}{d\theta_e} i_{s\alpha} + \frac{d\varphi_{r\beta}}{d\theta_e} i_{s\beta}] \quad (19)$$

where $\varphi_{r\alpha}$ and $\varphi_{r\beta}$ are the α and β axes rotor fluxes, respectively. The stator linkages are estimated from the measured stationary $\alpha - \beta$ reference frame [35]. The stator flux linkage and its vector position are given in Equations (20)–(22):

$$\varphi_{s\alpha} = V_{s\alpha} t - R_s \int i_{s\alpha} dt + \varphi_{s\alpha}(0) \quad (20)$$

$$\varphi_{s\beta} = V_{s\beta} t - R_s \int i_{s\beta} dt + \varphi_{s\beta}(0) \quad (21)$$

$$\theta_s = \tan^{-1} \frac{\varphi_{s\beta}}{\varphi_{s\alpha}} \quad (22)$$

where $\varphi_{s\alpha}(0)$ and $\varphi_{s\beta}(0)$ are the initial stator flux linkage values, which are given in Equation (23):

$$\varphi_{s\alpha}(0) = 0 \varphi_{s\beta}(0) = \frac{2K_b \pi}{3\sqrt{3}} \quad (23)$$

where K_b is the back emf constant, from the above equations, and the flux, torque, and sector angle are estimated [36].

4. Proposed Method

In this study, an EMS for an EV is developed. Its sources of energy are PV systems, batteries, and UCs, and its joining and converting components are power electrical circuits. Behind the MPPT control approach, the solar panel might collect solar energy throughout

the day to support the battery's energy costs. The battery would immediately supply the motor's energy needs, which call for a DC source. The battery's voltage drops very little, since the energy demand is so low when the automobile is in idle mode. The motor should produce a large current spike whenever the car is moving or ascending a slope. This current impulse could cause a significant voltage drop in the battery, affecting the DC outlet's ability to produce quality power. Additionally, battery life is shortened by a high current discharge. Therefore, one should connect the battery in conjunction to the UC and its bi-directional DC/DC converter. The UC is powering up to its applied value while the vehicle is in gear. A bi-directional DC/DC is regulated as a current source to deliver the additional load current during current pulses in order to keep the battery power from surpassing a predetermined level, preventing voltage drops, and extending battery life. Figure 4 displays the overall block diagram in its original form.

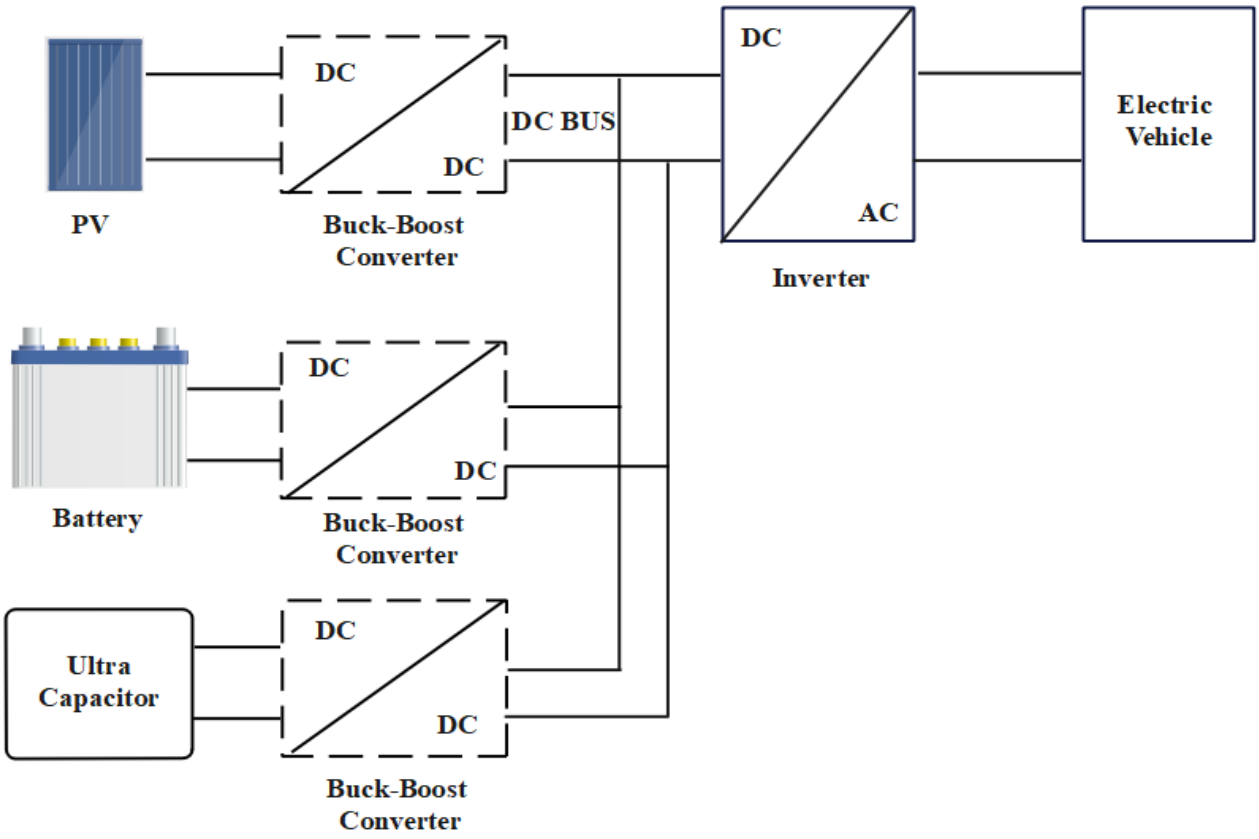

Figure 4. Overall block diagram of the analyzed EMS for an electric vehicle.

The MPPT operation to keep the battery charged is carried out via the boost converter. In the timespan of MPPT, the battery voltage is regarded as stable. Only the output current and voltage of the solar are taken into account when adjusting the boost converter's duty cycle. The motor is currently receiving direct power from the battery. A specific amount of energy is stored using the upper capacitor and the bi-directional buck-boost converter in the running phase and is discharged to provide impulse power in the accelerated and ascending slope modes.

An effective result with fewer and smaller external components is provided by buck-boost converters. With these few components, voltages can be stepped-up or stepped-down, and they also provide a shorter working duty cycle and improved efficiency over a wide range of input and output voltages. The DC/DC converter is employed when connecting a PV system to control the DC-link voltage and raise the voltage. To connect the UC module, however, a reversible DC/DC converter is required. There are many different DC/DC converter designs, such as direct energy conversion and appropriate storage component topologies.

Numerous benefits can be realized depending on how this energy system is set up. Initially, the battery could immediately charge the engine without worrying about a voltage drop, increasing efficiency. Moreover, battery life is prolonged since a significant current discharge is prevented. Third, if necessary, this device can also gather a lot of response energy by using a buck-boost converter to charge the top capacitor. Fourth, adding solar panels increases the capacity of electric vehicles to cruise by absorbing energy from the environment.

4.1. Processing Data by ANNs

In general, a pre-specified number of power measurements of the PV system are used in an ANN-based approach to automatically discover the global maximum power point of the PV array. The technology eliminates the need for extra sensors that would have provided data on the temperature of the PV modules and the operating parameters of the environment by just requiring the measurement of PV voltages and currents. The amount of time needed to generate the most power possible from the PV systems is roughly constant and predetermined. The capability of the ANN to achieve the maximum and its forecast accuracy increase with the number of power–voltage characteristic scansions. The algorithm is inexpensive, requires little extra equipment, and is only slightly dependent on changes in system parameters. The use of ANN models in the field of solar energy is constantly evolving, especially in relation to PV systems.

Under varied irradiation intensities, the partially shaded PV module receives a consistent amount of sunlight, while the shaded component receives very little. The partial circumstance is characterized as the proportion of irradiance on shaded to non-shaded segments, and its shaded ratio is established by the measuring of shaded portions. If a partial performance level is recognized, the shading factor is used to completely analyze this situation. Moreover, it is considered as the first step towards system monitoring and supervision. On the other hand, assessment and detection are accomplished using ANN agents.

A standard ANN consists of input, hidden, and output layers. The output of the j_{th} neuron from the hidden layer is calculated in Equation (24):

$$\varphi_j(x) = f_j\left(\sum_{i=1}^{n} W_{ji} X_i\right) \tag{24}$$

where $f_j(.)$ is the activation function for the j_{th} node in the hidden layer, and W_{ji} is the weight connecting the j_{th} hidden node with the i_{th} input X_i. In the output layer, the l_{th} network output is given in Equation (25):

$$Y_k = f_k\left(\sum_{j=1}^{n} W_{kj} \varphi_j(X)\right) \tag{25}$$

where the weight connecting the k_{th} output node with the j_{th} node in the hidden layer is specified as W_{kj}, and f_k is referred to as the activation function of the k_{th} node in the output layer. The cost function for the k_{th} sample data is described in Equation (26):

$$E_k = 0.5((Y_{Tk} - Y_k)^2) \tag{26}$$

where Y_{Tk} is the target output, and Y_k is the network output. After completing the training of an ANN, it could be utilized as a classifier to identify the section number for any specified shading configuration.

4.2. Processing Data with ANN in MATLAB

The robust functioning, rapid tracking, non-linear system endurance, and off-line training of ANN were all employed in this study. As a result, ANN-based PV MPPT approaches have lately become popular. NNs are black box machines that collect input and generate outputs without the need for a mathematical formula. Heating and irradiation are represented by two neurons in the input layer. Ten neurons with nonlinear activation functions are represented in the hidden layer; and just one neuron is represented in the

output layer. As a result, each input neuron communicates with all hidden layer neurons, but every hidden layer neuron interacts with both the output layer through weights, as shown in Figure 5.

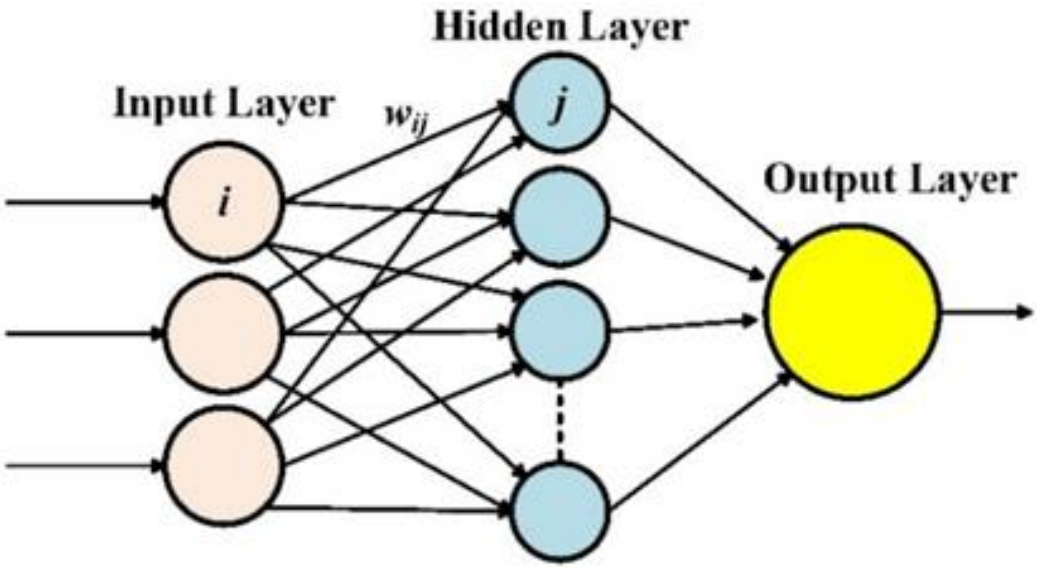

(**a**)

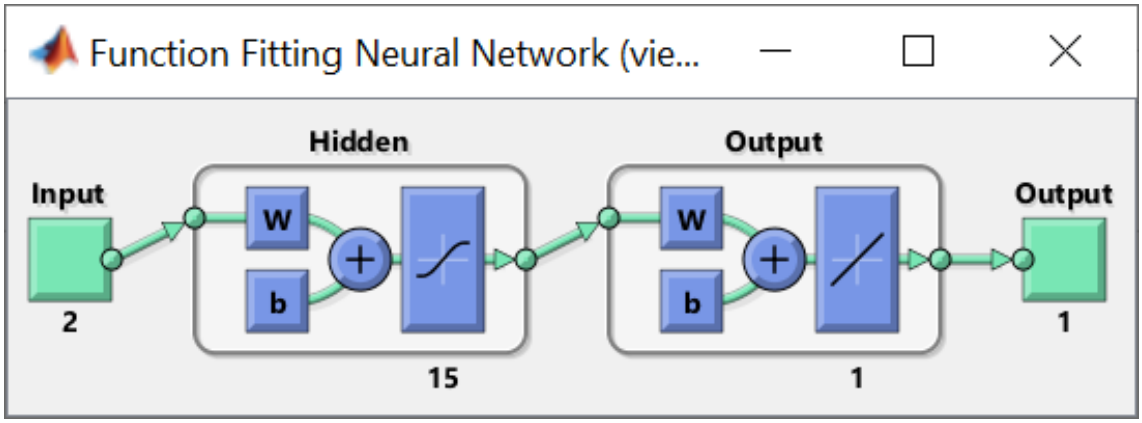

(**b**)

Figure 5. Modeling the tested NN: (**a**) configuration; (**b**) architecture of LM.

These weights are adjusted once the ANN has been trained to recognize the bi-directional causality among outputs and inputs. In addition to training the NN, the PV system modelling in MATLAB/Simulink with the Levenberg–Marquardt (LM) back-propagation technique was used to gather the data relating to the source and load. This algorithm was chosen due to the fact that when compared to conventional methods it has a faster convergence and higher accuracy. The output power is measured, along with the voltage related to the MPP for various combinations of temperature and irradiation. These data were exploited to train the network. Throughout the training stage, the "newff" function was utilized to stipulate the count of the layer's quantity, neurons, and activation function.

5. Aquila Optimizer Algorithm (AOA)

Here, the projected method, namely, the Aquila Optimizer (AO), is explained, formulated, and discussed.

5.1. Inspiration and Behavior

One of the most well-known raptors in the Northern Hemisphere is the Aquila. This type of hawk is one of the most widely spreading species. The Aquila is an example of a bird that is in the family "Accipitridae". Its typical color is dark brown, with lighter golden-brown feathers on its neck's backside. This type of Aquila's juveniles typically have faint white markings on their feathers and a white tail. The Aquila catch a variety of prey, primarily mice, squirrels, eidolons, beavers, raccoons, and other small mammals, using its quickness, flexibility, strong feet, and long, hooked claws. In the natural environment, the Aquila's specific behaviors are visible. They are known to primarily employ four different hunting techniques, each of which has a number of distinct advantages over the others. Depending on the circumstances, many Aquila can deftly and swiftly switch among various hunting techniques. In summary, this hawk is arguably the second-most knowledgeable and skilled hunter following humans themselves. This fact was the primary source of inspiration for the suggested AOA. Similar various activities were modeled in a simulation environment.

5.2. Initialization

The population of potential answers, given in Equation (27), is generated randomly from the upper bound (UB) and lower bound (LB) of the particular problem, which serves as the starting point for the optimization procedure in the population-based approach known as AOA. In every cycle, the best so-far-obtained answer is roughly considered to be the ideal solution.

$$X = \begin{bmatrix} x_{1,1} & \cdots & x_{1,j} & x_{1,Dim-1} & x_{1,Dim} \\ x_{2,1} & \cdots & x_{2,j} & \cdots & x_{2,Dim} \\ \cdots & \cdots & x_{i,j} & \cdots & \cdots \\ \vdots & \vdots & \vdots & \vdots & \vdots \\ x_{N-1,1} & \cdots & x_{N,1-j} & \cdots & x_{N-1,Dim} \\ x_{N,1} & \cdots & x_{N,j} & x_{N,Dim-1} & x_{N,Dim} \end{bmatrix} \quad (27)$$

The set of current candidate solutions, represented as X, are described in Equation (28), where X_i denotes the decision values of the i^{th} solution, N is referred to as the total number of candidates, and Dim specifies the dimension.

$$X_{ij} = rand \times \left(UB_j - LB_j\right) + LB_j\,,\ i = 1,\ 2,\ \ldots\ldots,\ N_j = 1,\ 2,\ \ldots..,\ Dim \quad (28)$$

The random number is denoted as $rand$, LB_j refers to the j^{th} LB, and UB_j refers to the j^{th} UB of the specified issue.

5.3. Mathematical Design

The suggested AOA method models the Aquila's behavior while hunting by acting out each stage of the hunt. The following sub-sections describe a suggested mathematical formula for the AO.

5.3.1. Exploration

In the first method (X_1), the Aquila can identify the target region and choose the optimum hunting location by swooping high in the air. Therefore, the AO broadly explores from a high transcend to pinpoint the hunt location, where the Aquila's fast soar with vertical stoop activity occurs. This pattern is expressed quantitatively in Equation (29):

$$X_1(t+1) = X_{best}\,(t) \times \left(1 - \frac{t}{T}\right) + \left(X_M\,(t) - X_{best}\,(t) * rand\right) \quad (29)$$

where $X_1(t+1)$ denotes the solution of subsequent iteration of t; $X_{best}\ (t)$ refers to the best-obtained result till the t^{th} iteration; $\left(\frac{1-t}{T}\right)$ is exploited to manage the exploration; and $X_M(t)$ refers the mean position that is computed in Equation (30):

$$X_M\ (t) = \frac{1}{N}\ \sum_{i=1}^{N} X_i\ (t),\ \forall_j = 1, 2 \ldots\ \ldots,\ Dim \tag{30}$$

5.3.2. Narrowed Exploration

In X_2, this activity is statistically described in Equation (31):

$$X_2 = (t+1) = X_{best}(t) \times Levy\ (D) + X_R\ (t) + (y - x) * rand \tag{31}$$

where $Levy\ (D)$ refers to the Levy flight distribution function, which is computed through Equation (32), where $X_{R(t)}$ is declared as a random solution obtained within $[1\ N]$ at the i^{th} iteration.

$$Levy\ (D) = s \times \frac{u \times\ \sigma}{|v|^{\frac{1}{\beta}}} \tag{32}$$

Constant s is set as 0.01, u and v are referred to as random figures among 0 and 1, and σ is considered by means of Equation (33):

$$\sigma = \left(\frac{\Gamma\ (1+\beta) \times \sin e\left(\frac{\pi\beta}{2}\right)}{\Gamma\left(\frac{1+\beta}{2}\right) \times \beta \times 2^{(\frac{\beta-1}{2})}} \right) \tag{33}$$

where β is equal to to 1.5. In Equation (31), y and x are exploited to offer the spiral shape, which are expressed in Equations (34) to (38):

$$y = r \times \cos(\theta) \tag{34}$$

$$x = r \times \sin(\theta) \tag{35}$$

where,

$$r = r_1 \times U \times D_1 \tag{36}$$

$$\theta = -\omega \times D_1 \times \theta_1 \tag{37}$$

$$\theta_1 = \frac{3 \times \pi}{2} \tag{38}$$

where r_1 lies between 1 and 20; U is equal to 0.00565; D_1 ranges from 1 to the length of the search space; and ω is equal to 0.005.

5.3.3. Exploitation

In exploitation, this activity is statistically processed as in Equation (39):

$$X_3\ (t+1) = (X_{best}\ (t) - X_M\ (t)) \times \alpha - rand + ((\ UB - LB) \times rand + LB) \times \delta \tag{39}$$

where $X_M\ (t)$ refers to the mean value of the present solution at the t^{th} iteration.

5.3.4. Narrowed Exploitation

In (X_4), this activity is statistically processed as in Equation (40):

$$X_4\ (t+1) = QF \times X_{best}(t) - (G_1 \times X\ (t) \times rand\ ) - G_2\ \times Levy\ (D) + rand \times G_1 \tag{40}$$

where G_1 refers to the AO movements and is expressed by Equation (42); G_2 ranges from 2 to 0 and is described in Equation (43):

$$QF(t) = \frac{2 \times rand - 1}{t^{(1-T)^2}} \tag{41}$$

$$G_1 = 2 \times rand - 1 \tag{42}$$

$$G_2 = 2 \times \left(1 - \frac{t}{T}\right) \tag{43}$$

where $QF(t)$ is given in (41), which is the function at the t^{th} iteration; t and T refer to the current and maximum iterations count, correspondingly.

An HESS encourages the use of PV energy generation and realizes the value that it adds. In order to ensure the system operates reliably, this research looks at ways to increase the charging station by introducing the objective function. The multi-objective capacity optimization configuration model's purpose is to establish the PV power, which is stated in Equation (44):

$$f_1 = \max(PV) = \frac{E_{HESS}}{\sum_{t=1}^{T} P_{PV}(t)} \tag{44}$$

Figure 6 displays the flowchart of the proposed ANN–AOA method.

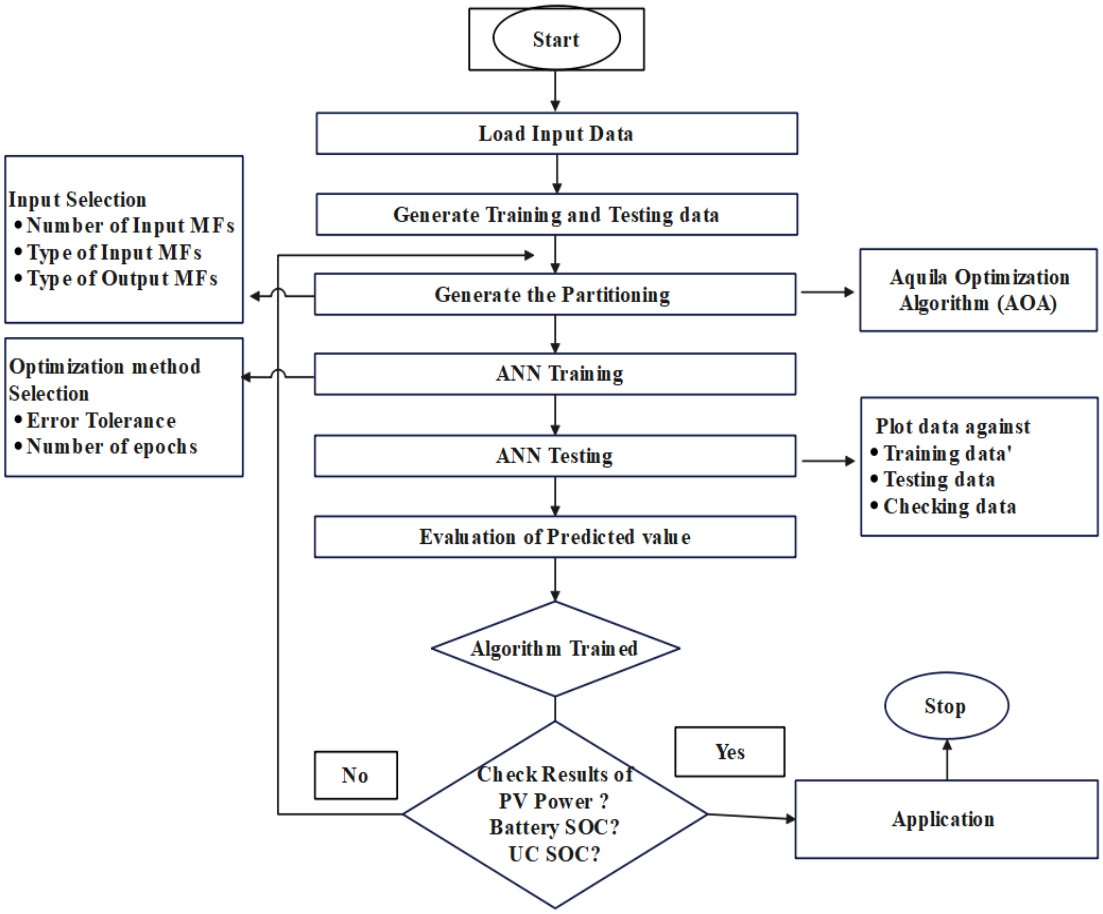

Figure 6. Flowchart of the proposed ANN–AOA method.

The proposed ANN–AOA method provides better results of PV power, battery SOC, and UC SOC at the end. Once the input is trained and tested with the ANN–AOA, the output is checked with the possible results, e.g., PV required to achieve the maximum peak power and also needed to sustain the SOC of both battery and ultracapacitor in order to maintain the energy management between the specified sources and the electric vehicle.

6. Results and Discussion

By utilizing the MATLAB/Simulink system model, results were produced to confirm the effectiveness of the suggested EMS and control system. The suggested ANN–AOA system's evaluation was carried out using the MATLAB program. The outcomes considering the battery, UC, and PMSM measurements are described in Table 1. For a constant load (i.e., PMSM) during a 200 s time period, the HESS value is presented. Torque, battery SOC, and motor RPM were all considered in the accomplishment of the suggested process. The Urban Dynamometer Driving Schedule (UDDS) driving cycle was employed to assess the performance of traction motor, which completely depends on vehicle ratings, such as the battery and drivetrain values [37].

Table 1. Overall results of the proposed ANN–AOA system.

Rating of Battery	Internal resistance	0.24691 (Ohms)
	Volumetric energy density	200–250 (Wh/L)
	Exponential zone	216.9492 (V), 1.62 (Ah)
	Fully Charged Voltage	235.5932 (V)
	Energy Capacity	7.7885 (Ah)
	Maximum capacity	8.7231 (Ah)
	Discharging current	50, 100 $[i_1, i_2]$ (A)
	Nominal discharge current	1.62 (A)
Rating of UC	Resistances $[R_1, R_2, R_3]$	0.2, 90,100 (Ohm)
	Initial Voltage	16 (V)
	Maximum Voltage	270 (V)
	Capacitances $[C_1, C_2, C_3]$	2.5, 1.5, 4 (F)
	Voltage dependent capacitor gain	0.95
Rating of PMSM	Armature inductance	0.000835 (H)
	Flux linkage	0.17566
	Number of pole pairs	4
	Power rating	50 (kW)
	Speed	3500 (rpm)
	Stator phase resistance	0.18 (Ohm)
	Voltage	500 (V)
Ratings of PV	Maximum generated power	305.226 (W)
	Light generated current	6.0092 (A)
	Diode current	$6.3014 \cdot e^{-12}$ (A)
	Ideality element	0.94504
	Cells per module	96 (N/cell)
	Open circuit voltage	64.2 (V)

The MATLAB simulation architecture of the ANN–AOA-driven HEV is shown in Figure 7. This includes the UC, Ni-MH battery, HEV, and ANN–AOA as its main components. As the primary source, the battery mainly provides the necessary energy to move the car. The UC is then employed whenever the battery's SOC is much less than 60%, and the ANN–AOA regulator is also used to manage it.

This paper provides some practical suggestions for enhancing the MPPT's functionality. Even though many MPPT strategies have been used up to this point, significant changes are always needed for MPPT to operate as efficiently as possible. Our study came to the conclusion that the suggested ANN–AOA works effectively under a consistent solar intensity.

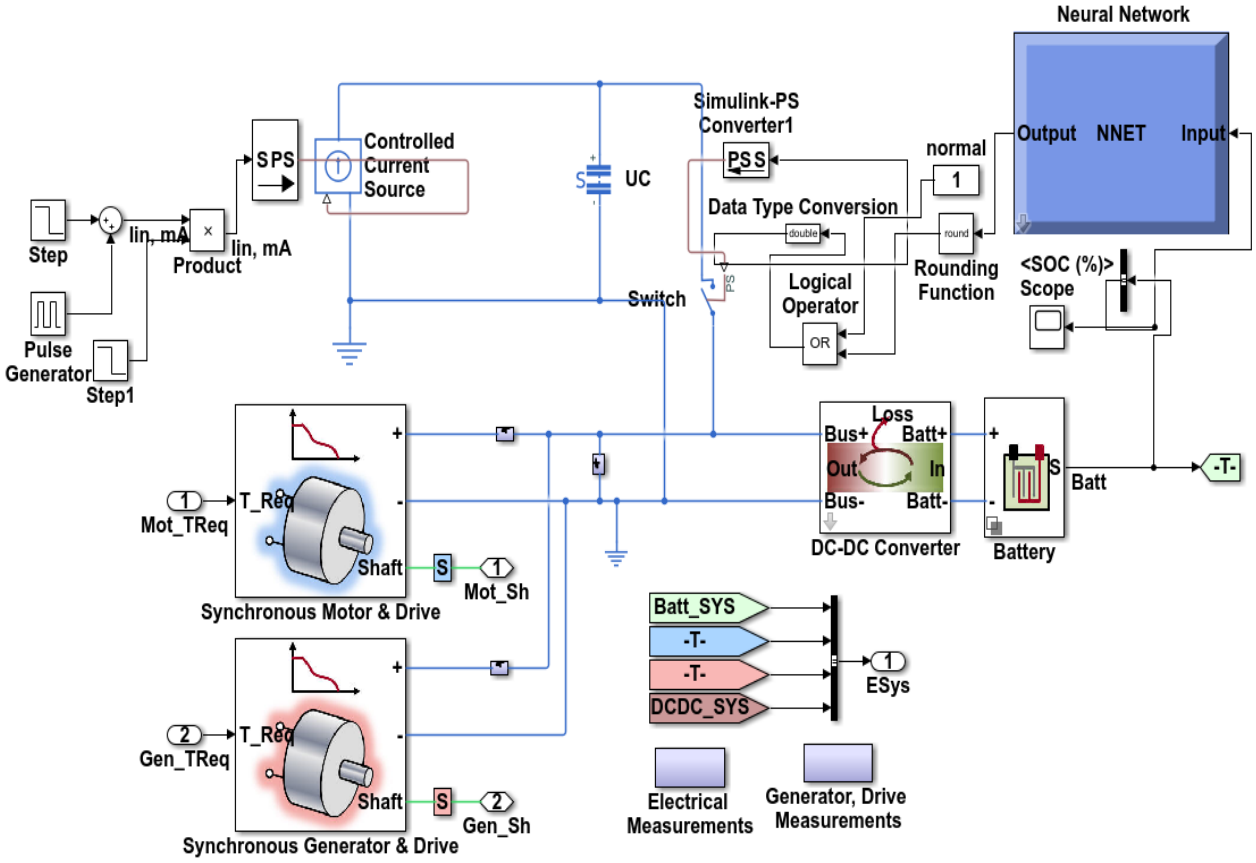

Figure 7. Simulation design of the proposed ANN–AOA method.

According to Figures 8–10, compared to other control schemes, the suggested technique collected the most power.

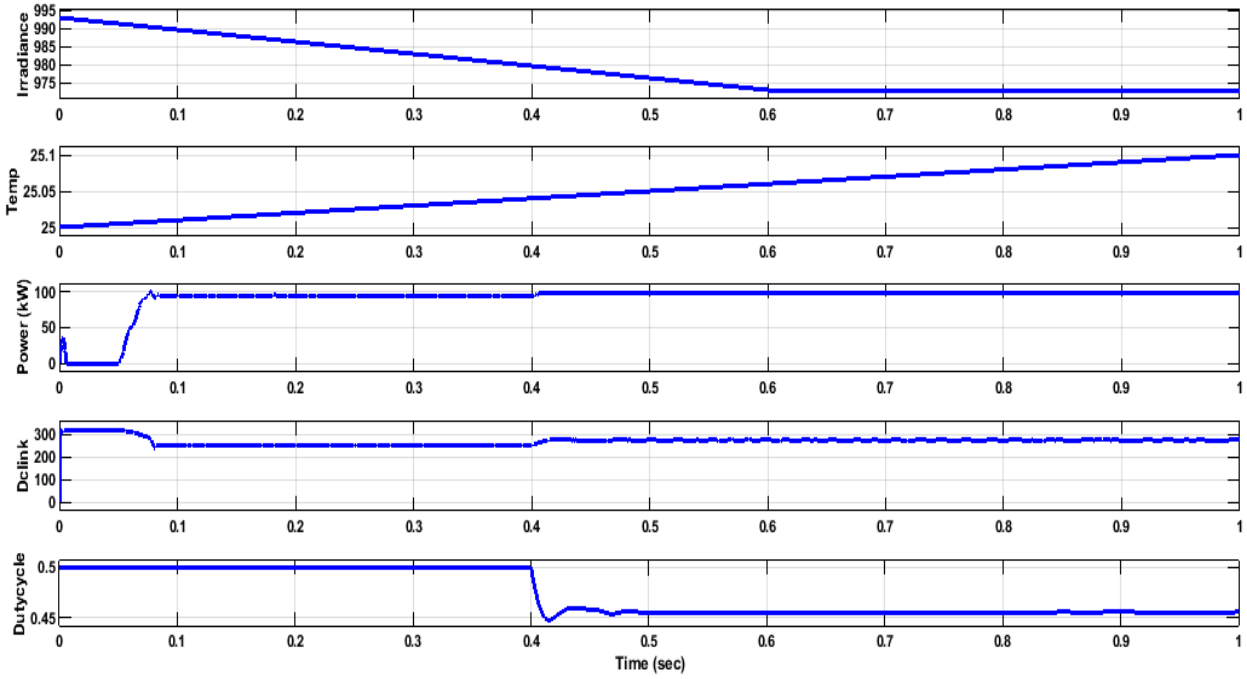

Figure 8. Performance analysis using the ANN method.

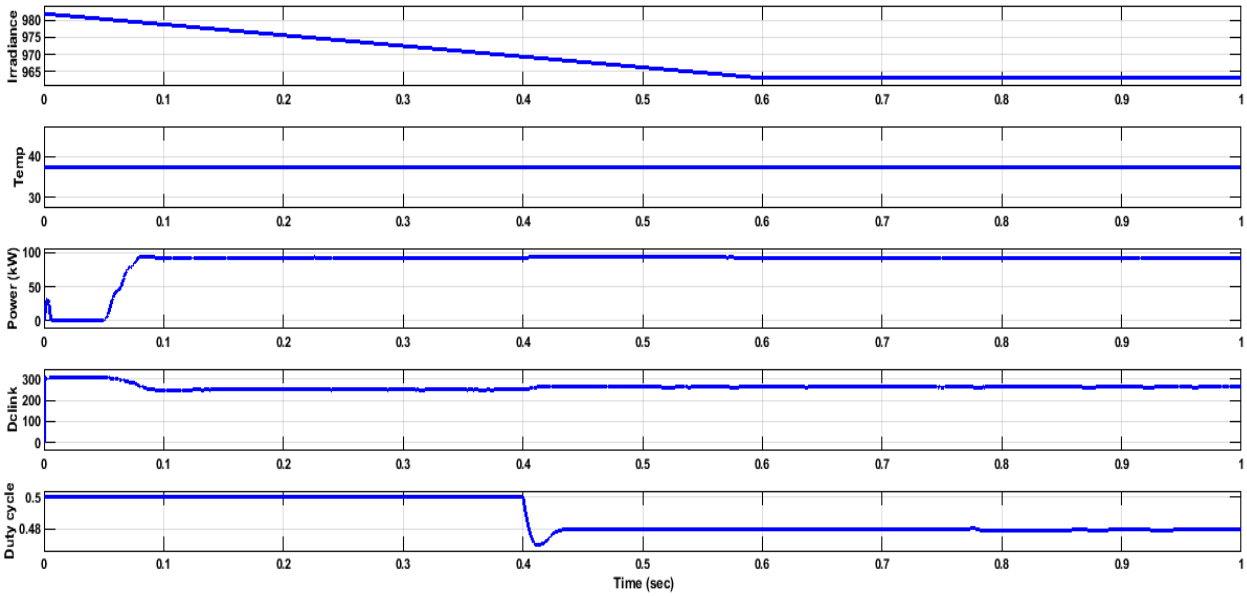

Figure 9. Performance analysis using the AOA method.

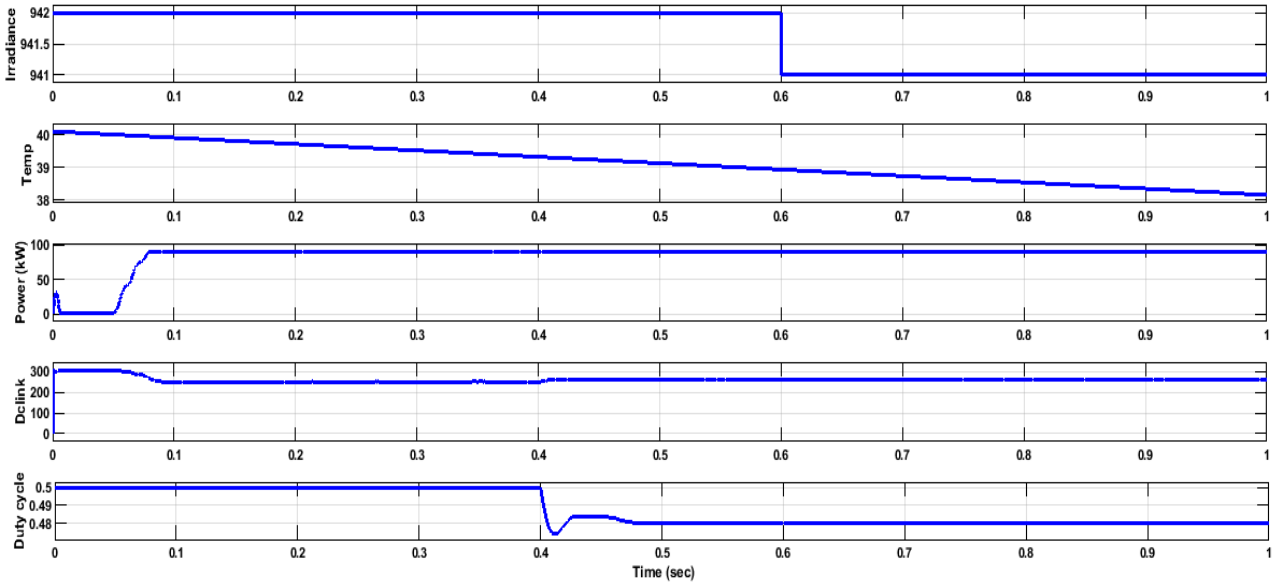

Figure 10. Performance analysis using the ANN–AOA method.

As summarized in Table 2, the suggested ANN–AOA method outperformed the separately employed ANN and AOA techniques by achieving a maximum output of 92.930 kW. The highest outputs extracted by the ANN and AOA were 88.209 kW and 90.238 kW, respectively.

Table 2. Analysis of PV power under various methodologies.

Techniques	PV Power (kW)
GA-PID [23]	89.259
MHS [26]	90.821
ANN method	90.357
AOA method	92.924
Proposed ANN–AOA method	95.752

While related with the current framework, this assortment offers minimal effort and smaller magnitude with supplementary working highlights such as voltage limit and enhanced speed. Energy density, power density, and productivity increased with the assistance of the previously stated ESS. Likewise, the comprehensive cost was additionally exceptionally less. The insurance of the battery and its expense was higher, since it was straightforwardly relative to the cost of advancement and capability. If the vehicles weight were to increase, the productivity would decrease, which raises the expense. The charging/releasing cycle was expanded by utilizing UC.

While the parameters were already explained in the previous section, the discharge characteristics of the NiMH battery's nominal current is shown in Figure 11. The SOC of a battery with and without ANN–AOA is shown in Figure 12.

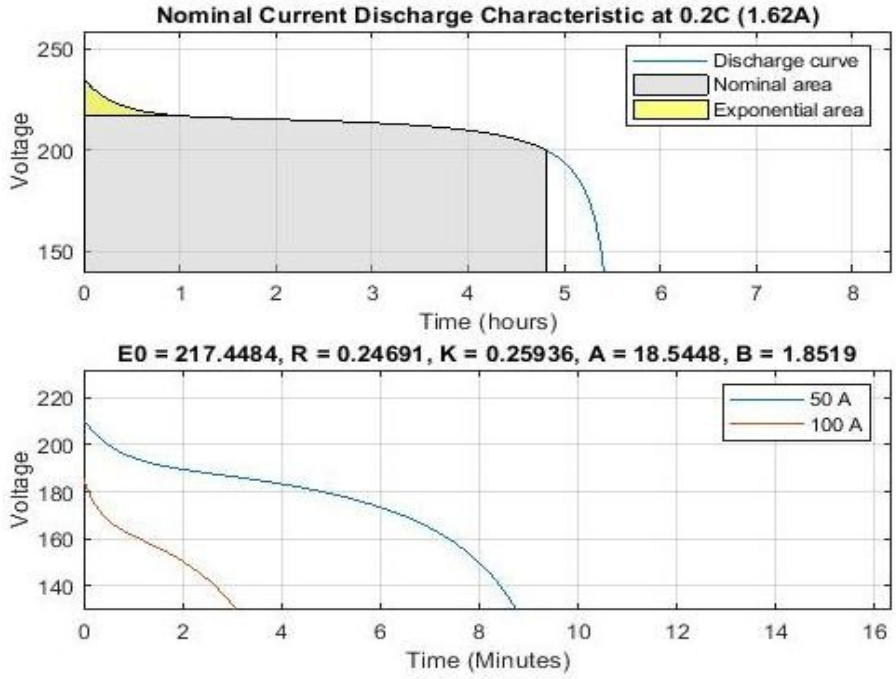

Figure 11. Characteristics of the discharge current of a NiMH battery.

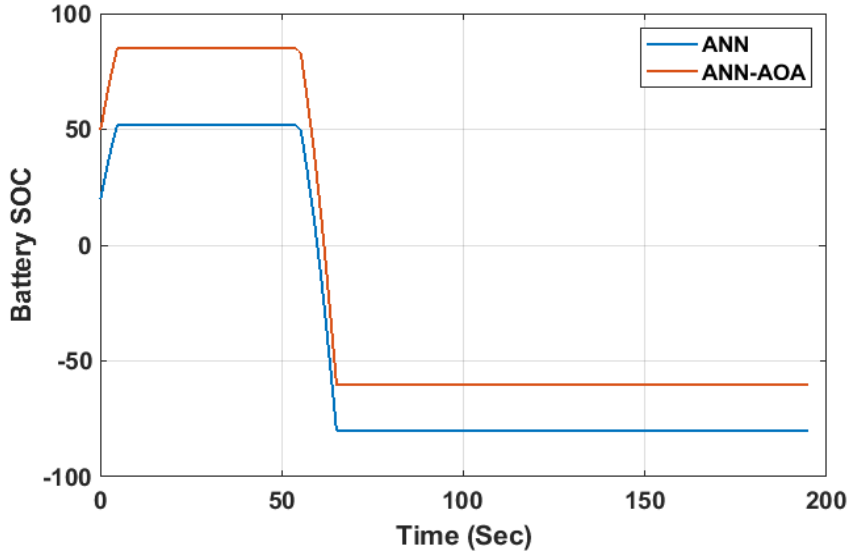

Figure 12. Analysis of SOC of a battery with and without ANN–AOA.

The battery's SOC estimate protects the device from unforeseen disruptions and guards against overcharging and over discharging that could damage the battery's internal structure. As seen in Figure 11, it was found that the ANN–AOA regulated the UC's charging and discharging features, which led to the development of the battery's SOC. Compared to other methods now in use, the ANN–AOA method had a longer lifespan. As shown in Figure 12, the battery's SOC was zero after 60 s. At that point, the ANN–AOA instructs UC to provide the HEV with the required power. The SOC of UC is shown in Figure 13.

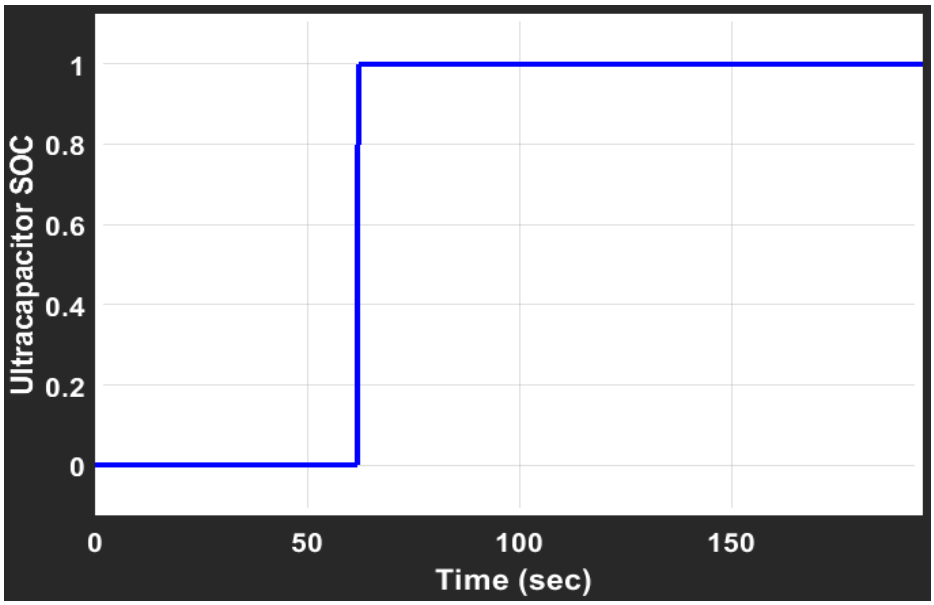

Figure 13. Analysis of SOC of UC with ANN–AOA.

The evaluation of engine speed with and without use of the ANN–AOA technique is shown in Figure 14, which depicts the level of speed that the PMSM motor can achieve. Without an approach, a motor's velocity is less closely tied to ANN–AOA. The ANN–AOA-dependent HESS vehicle speed is tied to a rule-based technique that was examined using two different segments: the Manhattan cycle, and the UDDS cycle.

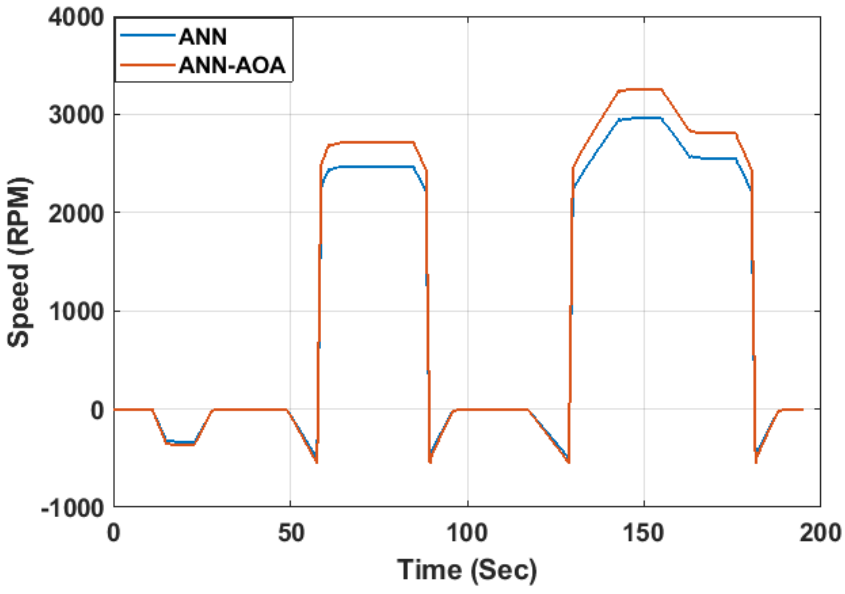

Figure 14. Analysis of motor speed with ANN and ANN–AOA.

The vehicle's speed, with and without the use of the ANN–AOA method, is shown in Figure 15.

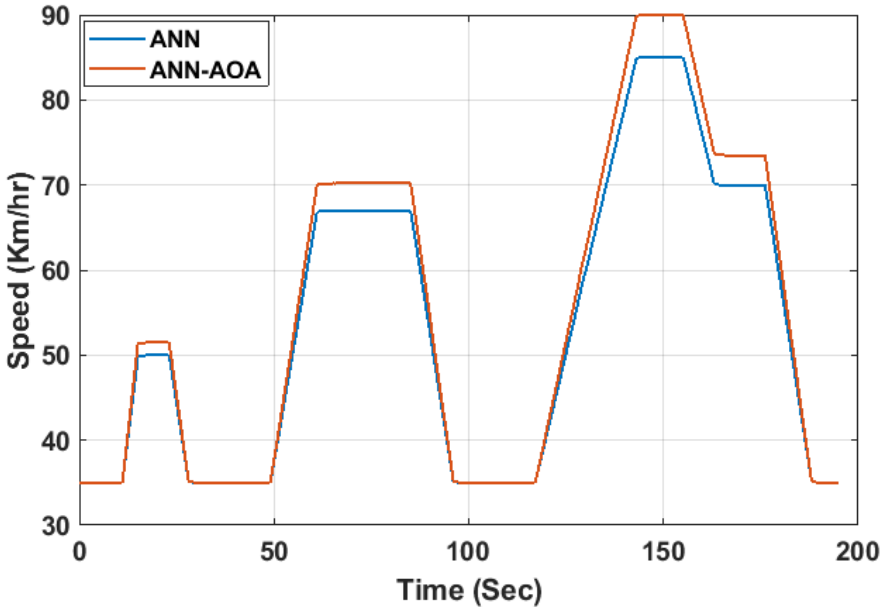

Figure 15. Analysis of vehicle speed with ANN and ANN–AOA.

When combined with HEV and without ANN–AOA, the speed could be more fully utilized. As described in Table 3, it is clear that ANN–AOA-based electric vehicles reached an extraordinary speed of 91 km/h, which is substantially faster than current techniques.

Table 3. Evaluation of vehicle speed under various methodologies.

Approaches	Maximum Speed of HEV (km/h)
ANN–AOA-based HEV	91
AOA-based HEV	86
ANN-based HEV	83
GA-PID [23]	84
MHS [26]	87

As the central component of this HESS, the bi-directional DC/DC converter management is the subject of this paper's numerical simulations. There is no emphasis on the boost circuit, although the energy from the solar array and its transport to the battery or demand is indeed significant in this study as a full system. This portion of the circuit's test findings that are easily understandable and realized are not displayed.

7. Conclusions

This study presents a hybrid energy system for an all-electric vehicle. The control technique is examined together with a topology for integrating the energy sources, namely, a solar panel, battery, and UC. The architecture uses the fewest possible electronic converters, reducing loss while enhancing EV efficiency and battery capacity. The suggested control approach is validated by the simulation results. As shown, large current battery discharge has been stopped. With the aid of the control methodology, switching between the UC charging and discharging states might also be realized seamlessly. While contrasted to the GA-PID and MHS algorithms that are already in use, the numerical simulations in MATLAB demonstrate that the suggested ANN–AOA approach is effective in anticipating the energy consumption for the next simultaneous interval and accomplishes the EV's faster speed of 91 km/h. In the future, the architecture of the proposed framework could be improved by adopting a hybrid optimization-based technique to further increase the

battery capacity of HEVs. Outcomes of our studies may aid numerous parties, including those from the automotive industry, as well as researchers and professionals involved in designing, maintaining, and evaluating a variety of energy sources, especially renewables.

Author Contributions: The paper's investigation, resources, data curation, writing—original draft preparation, writing—review and editing, and visualization were conducted by N.N. and R.S.R.K.N. The paper's conceptualization and software were conducted by U.R. The validation, formal analysis, methodology, supervision, project administration, and funding acquisition of the version to be published were conducted by P.F.-G. and P.B.D. All authors have read and agreed to the published version of the manuscript.

Funding: This research received no external funding.

Institutional Review Board Statement: Not applicable.

Informed Consent Statement: Not applicable.

Data Availability Statement: No new data were created or analyzed in this study. Data sharing is not applicable to this article.

Conflicts of Interest: The authors declare no conflict of interest.

References

1. Florin Andrei, R.; Livint, G.; Baciu, A. Analysis of hybrid energy storage systems based on photovoltaic panel, supercapacitors and battery for electric vehicles. *Environ. Eng. Manag. J.* **2020**, *19*, 121–129.
2. Dhananjay, K.; Nema, R.K.; Gupta, S. A comparative review on power conversion topologies and energy storage system for electric vehicles. *Int. J. Energy Res.* **2020**, *44*, 7863–7885.
3. Muhammad Kashif, A.; Armghan, H.; Ahmad, I.; Hassan, M. Multistage adaptive nonlinear control of battery-ultracapacitor based plugin hybrid electric vehicles. *J. Energy Storage* **2020**, *32*, 101813.
4. Saikumar, B.; Balamurugan, S. Review on non-isolated multi-input step-up converters for grid-independent hybrid electric vehicles. *Int. J. Hydrogen Energy* **2020**, *45*, 21687–21713.
5. Yujie, W.; Li, W.; Li, M.; Chen, Z. A review of key issues for control and management in battery and ultra-capacitor hybrid energy storage systems. *eTransportation* **2020**, *4*, 100064.
6. Rayhane, K.; Bacha, S.; Smaoui, M. Robust optimization based energy management of a fuel cell/ultra-capacitor hybrid electric vehicle under uncertainty. *Energy* **2020**, *200*, 117530.
7. Dinakaran, C.; Padmavathi, T. Performance evaluation on electric vehicle by solar photovoltaic system. *Int. J. Sci. Tech. Adv.* **2020**, *6*, 39–44.
8. Prem, P.; Sivaraman, P.; Sakthi Suriya Raj, J.S.; Jagabar Sathik, M.; Almakhles, D. Fast charging converter and control algorithm for solar PV battery and electrical grid integrated electric vehicle charging station. *Automatika* **2020**, *61*, 614–625. [CrossRef]
9. Machlev, R.; Zargari, N.; Chowdhury, N.R.; Belikov, J.; Levron, Y. A review of optimal control methods for energy storage systems-energy trading, energy balancing and electric vehicles. *J. Energy Storage* **2020**, *32*, 101787. [CrossRef]
10. Wang, S.; Lu, L.; Han, X.; Ouyang, M.; Feng, X. Virtual-battery based droop control and energy storage system size optimization of a DC microgrid for electric vehicle fast charging station. *Appl. Energy* **2020**, *259*, 114146. [CrossRef]
11. Sujitha, N.; Subramanian, K. Off-board electric vehicle battery charger using PV array. *IET Electr. Syst. Transp.* **2020**, *10*, 291–300.
12. Lei, S.; Cheng, Q.; Cheng, Y.; Wei, L.; Wang, Y. Hierarchical control of DC micro-grid for photovoltaic EV charging station based on flywheel and battery energy storage system. *Electr. Power Syst. Res.* **2020**, *179*, 106079.
13. Kamaraj, V.; Nallaperumal, C. Modified multiport Luo converter integrated with renewable energy sources for electric vehicle applications. *Circuit World* **2020**, *46*, 125–135. [CrossRef]
14. Rahman, A.; Ahmad, I.; Shafiq Malik, A. Variable structure-based control of fuel cell-supercapacitor-battery based hybrid electric vehicle. *J. Energy Storage* **2020**, *29*, 101365. [CrossRef]
15. Maheswari, L.; Sivakumaran, N.; Balasubramanian, K.R.; Saravana Ilango, G. A unique control strategy to improve the life cycle of the battery and to reduce the thermal runaway for electric vehicle applications. *J. Therm. Anal. Calorim.* **2020**, *141*, 2541–2553. [CrossRef]
16. Han, X.; Liang, D.; Wang, H. An optimization scheduling method of electric vehicle virtual energy storage to track planned output based on multiobjective optimization. *Int. J. Energy Res.* **2020**, *44*, 8492–8512. [CrossRef]
17. Pranav, M.; Chaturvedi, P.; Gajbhiye, S. Enhanced control and dynamic power management of Li-Ion battery and ultracapacitor for hybrid energy storage system. In *Advances in Control Systems and Its Infrastructure*; Mehta, A., Rawat, A., Chauhan, P., Eds.; Springer: Singapore, 2020; Volume 604, pp. 97–108.
18. Kumaresan, J.; Govindaraju, C. Development of a power management algorithm for PV/battery powered plug-in dual drive hybrid electric vehicle (DDHEV). *Electr. Power Compon. Syst.* **2020**, *48*, 1–2, 70–85.

19. Raghavaiah, K.; Gorantla, S. Optimal performance of Lithium-Ion battery and ultra-capacitor with a novel control technique used in e-vehicles. *J. New Mater. Electrochem. Syst.* **2020**, *23*, 139–150.
20. Liu, J.; Dai, Q. Optimization of hybrid energy storage capacity for electric vehicle photovoltaic charging stations based on multi-objective quantum particle swarm optimization. *Acad. J. Eng. Technol. Sci.* **2020**, *3*, 26–39.
21. Zineb, C.; Batool, D.; Kim, J.; Yoo, K. Design and simulation studies of battery-supercapacitor hybrid energy storage system for improved performances of traction system of solar vehicle. *J. Energy Storage* **2020**, *32*, 101943.
22. Murat Mustafa, S.; Atay, A. Multiport bidirectional DC–DC converter for PV powered electric vehicle equipped with battery and supercapacitor. *IET Power Electron.* **2020**, *13*, 3931–3939.
23. Hocine, G.; Allaoui, T.; Mekki, M.; Denai, M. Power management and control of a photovoltaic system with hybrid battery-supercapacitor energy storage based on heuristics methods. *J. Energy Storage* **2021**, *39*, 102578.
24. Fares, A.M.; Klumpner, C.; Sumner, M. A novel multiport DC-DC converter for enhancing the design and performance of battery-supercapacitor hybrid energy storage systems for unmanned aerial vehicles. *Appl. Sci.* **2022**, *12*, 2767. [CrossRef]
25. Kachhwaha, A.; Izat Rashed, G.; Ranjan Garg, A.; Mahela, O.P.; Khan, B.; Badeaa Shafik, M.; Hussien, M.G. Design and performance analysis of hybrid battery and ultracapacitor energy storage system for electrical vehicle active power management. *Sustainability* **2022**, *14*, 776. [CrossRef]
26. Al-Dhaifallah, M.; Ziad, M.A.; Alanazi, M.; Dadfar, S.; Hosein Fazaeli, M. An efficient short-term energy management system for a microgrid with renewable power generation and electric vehicles. *Neural. Comput. Appl.* **2021**, *33*, 16095–16111. [CrossRef]
27. Katuri, R.; Gorantla, S. Math function-based controller combined with PI and PID applied to ultracapacitor based solar-powered electric vehicle. *Afr. J. Sci. Technol. Innov. Dev.* **2021**, *13*, 509–526. [CrossRef]
28. Suresh, K.; Sampath, H.; Chellammal, N.; Jondhale, S.R.; Bharatiraja, C. Modular multi-input bidirectional DC to DC converter for multi-source hybrid electric vehicle applications. *J. Appl. Sci. Eng.* **2021**, *25*, 389–399.
29. Małkowski, R.; Jaskólski, M.; Pawlicki, W. Operation of the hybrid photovoltaic-battery system on the electricity market-Simulation, real-time tests and cost analysis. *Energies* **2020**, *13*, 1402.
30. Nasser, K.W.; Yaqoob, S.J.; Hassoun, Z.A. Improved dynamic performance of photovoltaic panel using fuzzy logic-MPPT algorithm. *Indones. J. Electr. Eng. Comput. Sci.* **2021**, *21*, 617–624. [CrossRef]
31. Senthilkumar, S.; Mohan, V.; Mangaiyarkarasi, S.P.; Karthikeyan, M. Analysis of single-diode PV model and optimized MPPT model for different environmental conditions. *Int. Trans. Electr. Energy Syst.* **2022**, *2022*, 4980843. [CrossRef]
32. Rosiński, W.; Potrykus, S.; Michna, M. Design of battery charging system update for glider launcher. *Arch. Electr. Eng.* **2022**, *69*, 259–269.
33. Potrykus, S.; Kutt, F.; Nieznański, J.; Fernandez Morales, F.J. Advanced Lithium-Ion battery model for power system performance analysis. *Energies* **2020**, *13*, 2411. [CrossRef]
34. Bartłomiejczyk, M.; Jarzebowicz, L.; Kohout, J. Compensation of voltage drops in trolleybus supply system using battery-based buffer station. *Energies* **2022**, *15*, 1629. [CrossRef]
35. Kurpiel, W.; Deja, P.; Polnik, B.; Skóra, M.; Miedziński, B.; Habrych, M.; Debita, G.; Zamłyńska, M.; Falkowski-Gilski, P. Performance of passive and active balancing systems of Lithium batteries in onerous mine environment. *Energies* **2021**, *14*, 7624. [CrossRef]
36. Szymański, J.R.; Żurek-Mortka, M.; Wojciechowski, D.; Poliakov, N. Unidirectional DC/DC converter with voltage inverter for fast charging of electric vehicle batteries. *Energies* **2020**, *13*, 4791. [CrossRef]
37. Huynh, T.A.; Hsieh, M.F. Performance analysis of permanent magnet motors for electric vehicles (EV) traction considering driving cycles. *Energies* **2018**, *11*, 1385. [CrossRef]